

Pushing the limits of optical information storage using deep learning

Peter R. Wiecha,^{1,*} Aurélie Lecestre,² Nicolas Mallet,² and Guilhem Larrieu²

¹*CEMES, Université de Toulouse, CNRS, Toulouse, France*

²*LAAS, Université de Toulouse, CNRS, INP, Toulouse, France*

Diffraction drastically limits the bit density in optical data storage. To increase the storage density, alternative strategies involving supplementary recording dimensions and robust read-out schemes must be explored. Here, we propose to encode multiple bits of information in the geometry of subwavelength dielectric nanostructures. A crucial problem in high-density information storage concepts is the robustness of the information readout with respect to fabrication errors and experimental noise. Using a machine-learning based approach in which the scattering spectra are analyzed by an artificial neural network, we achieve quasi error free read-out of 4-bit sequences, encoded in top-down fabricated silicon nanostructures. The read-out speed can further be increased exploiting the RGB values of microscopy images, and the information density could be increased beyond current state of the art. Our work paves the way towards high-density optical information storage using planar silicon nanostructures, compatible with mass-production ready CMOS technology.

Optical information storage promises perennial longevity, high information densities and low energy consumption compared to magnetic storage media.^{1,2} The compact disc (CD) and its successors, the DVD and the blue-ray disc, broadly established optical storage in our society.^{3,4} Those media are based on storing a single binary digit per diffraction limited area (“zero” or “one”). Several concepts have been proposed to increase the information density in optical storage. Examples are schemes exploiting polarization-sensitive digits,⁵ near-field optical recording,⁶ the use of fluorescent dyes⁷ or three-dimensional approaches like two-photon point-excitation⁸. Yet, all these alternatives suffer from major drawbacks. Either they are hardly superior to commercial planar solutions (polarization-sensitive patterns) or they require very complex storage media (fluorescence) or sophisticated read-out schemes (near-field recording, two-photon point-excitation). The most promising alternative seemed to be holographic memory, which was proposed in the early 1960ies and makes use of the whole volume of the storage medium. To date, however, there is still no commercial product available, despite several announcements in the past 20 years.^{9,10}

In the last decades, photonic nanostructures emerged as powerful instruments to control light at the nanometer scale.^{11,12} Localized surface plasmons (LSP) in metal nanoparticles¹³ or Mie-type resonances in high-index dielectric structures¹⁴ cover the entire visible spectrum and can be tuned by designing appropriate geometric features.^{15,16} Furthermore, the high scattering efficiencies of photonic nanostructures render single-particle spectroscopy relatively easy. In consequence, the idea has been raised to encode information in the rich scattering spectra of plasmonic nanostructures, denser than a single data bit.^{17–21} The information density might be even further increased by addressing layer-wise arranged nanostructures via the focal depth²² or by the polarization of

the probe light²³. A key problem of such approach is the availability and accuracy of read-out schemes.^{18,24} The main difficulty consists in the fact that different nanostructure geometries can lead to quite similar optical responses, which need to be unambiguously identified during the information retrieval.^{18,25} This problem is further complicated by structural defects of the fabricated particles and by the noise generated during the optical detection. Further drawbacks are associated with the metallic character of plasmonic nanostructures. One problem is the limited scalability of the production. Another inconvenience with gold (the most common plasmonic material) is the limitation to wavelengths above the interband transitions, hence larger than ≈ 520 nm. Shorter wavelengths cannot be used to encode information, which effectively reduces the attainable information density.

To overcome all of these limitations, we develop here a scheme for digital information encoding, based on silicon nanostructures. Owing to its high refractive index with low imaginary part, silicon gives rise to nanostructures with low-loss optical resonances, tunable over the entire visible spectral range.^{14,16,26} In addition, silicon has great technological advantages, first of all the mass-production ready, high-precision CMOS based processing technology, and of course its low cost and durability. To reliably retrieve the stored information, we propose a machine learning (ML) based approach, in which the scattering spectra are analyzed by an artificial neural network (ANN). Artificial (or “deep”) neural networks are computational schemes that can be “trained” to efficiently solve problems, hard for classical computer arithmetics.^{27,28} ANNs are used in many every-day applications ranging from spelling correction, sentence completion and speech recognition in modern smartphones over automatic image tagging in social networks to medical image interpretation.^{29,30} Besides a few recent examples, ML is being scarcely applied on problems in nano-optics. In one work, robust data read-out from holographic memory was realized using convolutional ANNs.³¹ In another recent publication, anthrax spores were classified from microscopy images using deep neural networks.³² It has

* e-mail : peter.wiecha@cemes.fr

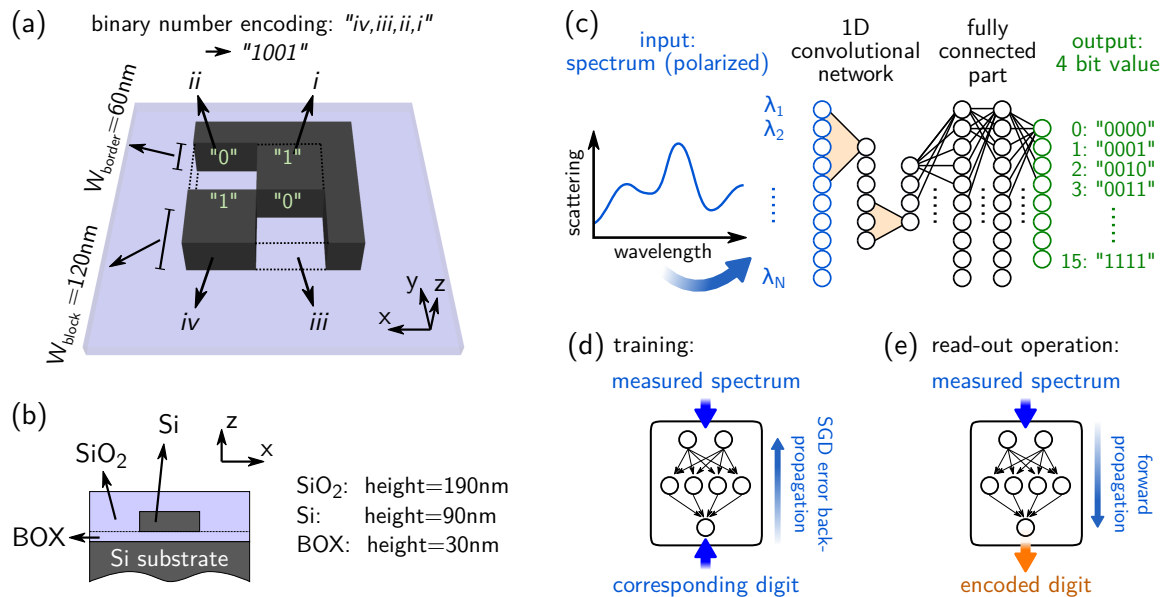


FIG. 1. **Sketch of the structure geometry and the 1D convolutional artificial neural network.** (a) shows an illustration of the “4 bit” nanostructure geometry. The digital information is encoded in the four silicon blocks (block: “1”, no block: “0”). The shown structure corresponds to the digit “1001” (decimal “9”). The L-shaped sidewall is necessary to distinguish symmetric arrangements via polarized optical spectroscopy. Each block occupies an area of $120 \times 120 \text{ nm}^2$. The L-shaped wall is 60 nm wide. The height is 90 nm. (b) side-view of the fabricated structure layout. (c) sketch of the 1D convolutional neural network used for the classification task. (d) training stage of the artificial neural network: measured spectra and corresponding digital information are fed into the network. The error is back-propagated using a variant of the stochastic gradient descent (SDG) algorithm. (e) the trained network is capable to retrieve the digital information encoded in the structures via their spectra.

also been shown recently on simple geometrical models, that ML can be used to inverse-design a nanostructure in order to yield a predefined optical response.^{33,34} To train the digital-information retrieval neural network, we fabricate several hundred copies of each nanostructure corresponding to a binary sequence. We then train an ANN on the individually measured scattering spectra. On our test dataset for structures encoding 4-bit of information, the trained network yields an error-free read-out. We demonstrate that it is sufficient for an accurate retrieval ($< 1\%$ error rate) to use the RGB color values from dark-field (DF) microscopy images. The latter approach allows a massively parallel read-out of the stored data. We finally show on a dataset generated from numerical simulations, that an accurate information retrieval is possible for binary sequences of at least 9 bits per diffraction limited area, effectively going beyond the data density of the blue-ray disc.

I. SILICON NANOSTRUCTURES FOR DIGITAL INFORMATION ENCODING

As illustrated in figure 1a, we use a checkerboard kind of array to encode several bits of information in the geometry of a silicon nanostructure. If at a certain position

in the 2D array a silicon block exists, the according bit is set to “1”. If there is no silicon, it is “0”. In order to unambiguously distinguish symmetric or rotational arrangements like binary numbers with a single bit (for example “0001” and “0100”), an L-shaped silicon frame is added, surrounding two sides of the structure. In this way, under linearly polarized illumination each binary number yields a unique spectral response.

For our demonstration we fabricate nanostructures consisting of 2×2 arrays of silicon blocks, hence encoding 4 bits of information ($\rightarrow 16$ possible permutations). Each block has a size of $120 \times 120 \times 90 \text{ nm}^3$ ($L \times W \times H$), the L-shaped sidewall has a width and height of 60 nm, respectively 90 nm. The planar silicon structures are fabricated by electron-beam lithography and subsequent dry-etching of commercial silicon-on-insulator (SOI) substrates with a silicon overlayer of $H = 90 \text{ nm}$ height. Subsequent to the etching, the structures are covered by a protective SiO_2 layer of 190 nm height. Embedding the structures in SiO_2 increases the intensity of the backscattered light, compared to nanostructures lying on a dielectric substrate in vacuum. A sketch of the vertical structure of the sample is shown in figure 1b. For more details on the fabrication process, see the Methods section.

We fabricate 550 copies of each binary number nanostructure. Using an automated setup with an XY piezo

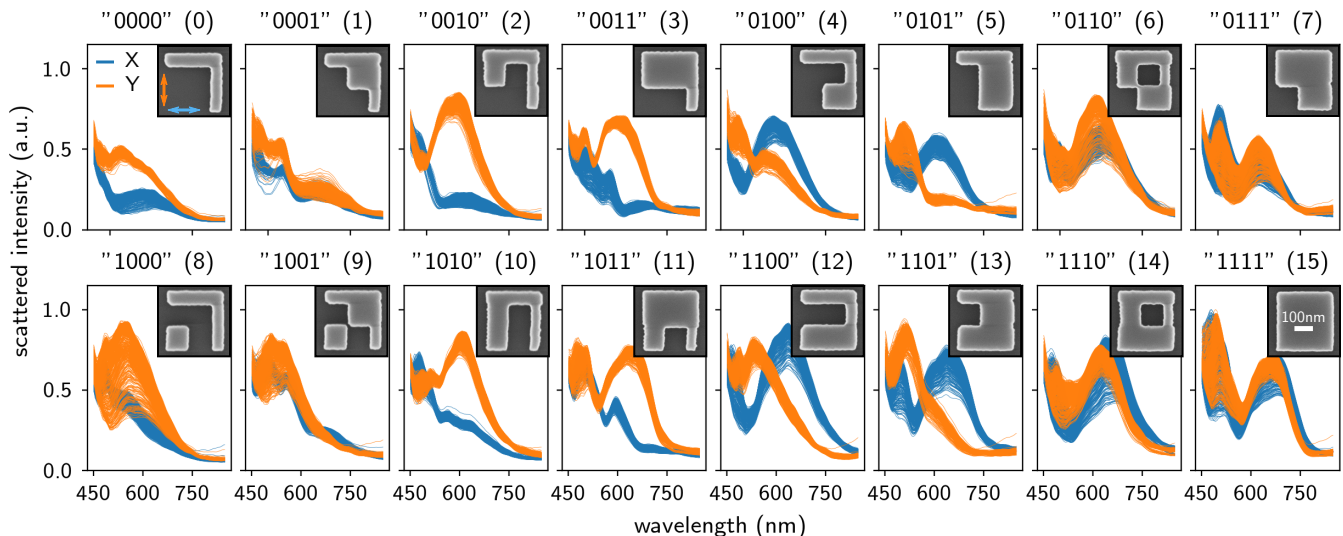


FIG. 2. **Experimental dark-field spectra training data-set.** Our data comprises measurements from 550 copies for each of the 16 “4 bit” geometries (this makes a total of 17600 acquired spectra). The spectra are superposed above each other. Blue lines: DF scattering for X -polarized light, orange lines: Y -polarization. Insets show SEM images of one representative copy of the respective nanostructure, the areas are $385 \times 385 \text{ nm}^2$, scalebar in “1111” is 100 nm.

stage, we measure the linearly X and Y polarized DF spectra of each of the $550 \times 16 = 8800$ fabricated structures, which gives us a dataset consisting of 17600 spectra. All acquired spectra are shown in figure 2, superposed and grouped by the 16 digital numbers. Scanning electron microscopy (SEM) images of selected copies of each digital structure are shown in the insets of figure 2. We note that the spectra of symmetric structures are not completely identical for crossed polarizations (see *e.g.* “0000”). We attribute this observation to the lithography in the fabrication process in which the electron-beam is raster scanned horizontally to develop the resist. This leads to slight differences (about 5 – 10%) between horizontal and vertical features in the structures (see also further SEM images in the [supporting informations](#)).

II. MACHINE LEARNING BASED DIGITAL INFORMATION READ-OUT

A. Read-out using scattering spectrum

Our goal is to read the information, encoded in the geometries of the silicon structures via a far-field optical measurement scheme. The optical scattering spectrum is a promising physical quantity to differentiate between the different structures, in other words to retrieve the bit-sequences they represent. We propose a machine-learning approach to the problem. We train an artificial neural network using a sub-set of the acquired spectra (data from 4800 structures). Subsequent to the training step, we evaluate the accuracy of the read-out scheme by testing the trained ANN with the remaining spectra

(4000 structures).

1. Network architecture

We use a one-dimensional convolutional neural network (ConvNet), followed by a fully connected network, as depicted in figure 1c. Such networks (ConvNet + fully connected part) are particularly strong in pattern-recognition tasks.²⁸ The spectra are fed in the network input layer which consists of one or two parallel channels, depending on the input data: One channel when using spectra of a single polarization, two channels when training with both polarizations. The 16 binary numbers are attributed to the “softmax” output layer which hence consists of 16 neurons. During training the neuron whose index corresponds to the input binary number is set to “1” while the other neuron activations are kept at “0”. Details on the network and training parameters as well as on the preprocessing of the data can be found in the Methods section. The categorical cross-entropy loss-function and the error rate on the validation set are shown in figure 3a for the first 100 epochs³⁵ of training.

2. Results

The read-out scheme is illustrated in Fig. 1e: The scattering spectra of the binary structures are fed into the trained ANN and forward propagated through the network. The output neuron with the highest activation in the final “softmax” layer indicates the encoded bit sequence. The read-out accuracy of the network trained

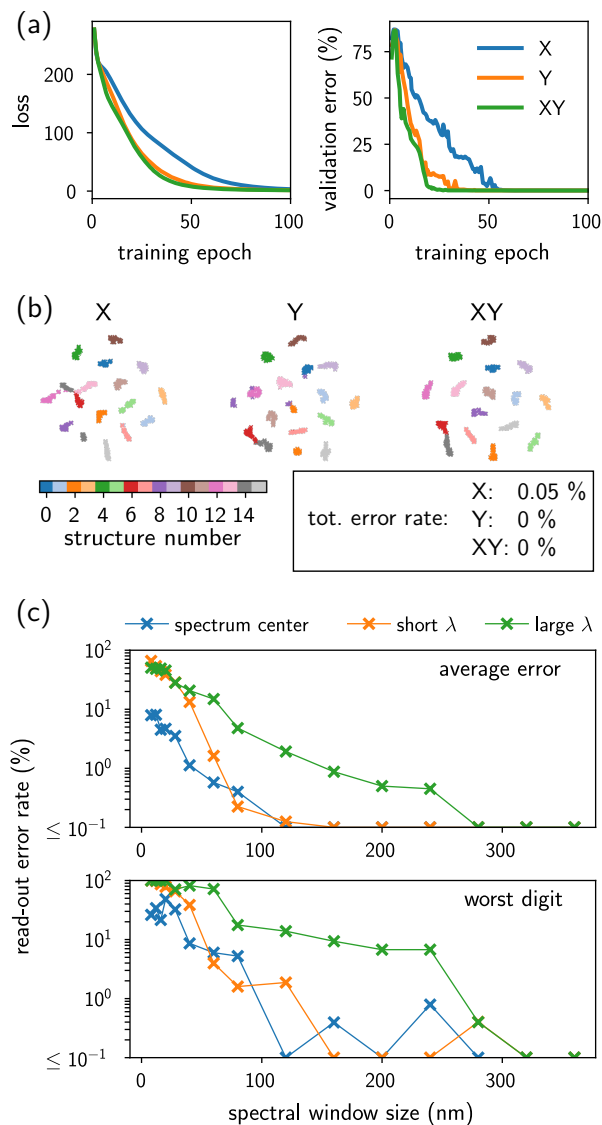


FIG. 3. **Training convergence and read-out accuracy of the ANN trained on the scattering spectra data.** (a) convergence of training. Loss (left) and validation error rate (right) as function of the training epoch. (b) t-SNE³⁶ visualization (see also text) of the three training sets. Left to right: Only X -polarization data, only Y -polarization and both together. Box on the right: read-out error rate of the network after training for 200 epochs for the three datasets. (c) read-out error as function of the spectral window size used from the training spectra (on the “XY” dataset). The spectral window was set either on the center of the acquired wavelength range (blue lines), from 450 nm upwards (orange lines) or starting from 850 nm towards shorter λ (green lines). The full acquired spectra have a spectral window of 400 nm, ranging from 450 nm to 850 nm (see also Fig. 2).

either only with spectra for X polarization, only with Y polarization or with both polarizations simultaneously is shown in figure 3b in the box at the right. Regardless the polarization configuration, the network is able to recog-

nize all 4000 test-structures – which it has never “seen” during training. The only exceptions are two incorrectly classified structures in the X -polarization case, which results in an 0.05% error rate. The spectra of the two erroneously retrieved structures are shown in the [supporting informations](#).

We analyzed the datasets using the “t-SNE” dimensionality reduction method.³⁶ In a t-SNE plot, well separated scatter points correspond to unambiguously different entities in the dataset. Nearby and overlapping points on the other hand correspond to very similar data. The results are shown in figure 3b. Each color corresponds to one of the binary structures, each dot represents the measurement from one specific copy. Obviously, all three datasets (Y , X and XY) are characterized by a very good separation of the different structure spectra in the t-SNE plots. It is thus not surprising that the ANN can retrieve the binary information with almost not errors.

To assess the amount of required information for an accurate information retrieval, we train and test the neural network with subsets of the original spectra. Figure 3c shows the classification error rate as function of the spectral window width used for training and retrieval (on the “XY” dataset). The top plot shows the average error on the whole test-set of 4000 structures, the bottom plot shows the error rate for the worst binary number. We evaluated three different positions of the spectral window: Either the window is taken up to the long wavelength end of the spectra ($\lambda \leq 850$ nm, green lines), or down to the short wavelength side ($\lambda \geq 450$ nm, orange lines), or it is centered around 650 nm (blue lines). We observe that the large wavelengths require a spectral window of ≈ 300 nm for good accuracy. We conclude that the red part of the spectra contains the least amount of information, not sufficient to unambiguously distinguish between the binary sequences. In the case of the central and blue sub-sets on the other hand, the read-out error decreases very rapidly, yielding error rates $\ll 1\%$ already for spectral windows of $\Delta\lambda \approx 100$ nm. We note that the amount of “information” contained in the scattering intensities at longer wavelengths could be increased by enlarging the nanostructures (e.g. increase the height), which would redshift the optical resonances.

B. Read-out using RGB color from microscope camera image

Obviously, a small spectral window is sufficient for very accurate information retrieval. Therefore, we will study if the binary digits can be recovered also using a simpler and faster data acquisition scheme. To this end, we use the scattered RGB color information from the nanostructures, obtained from conventional dark-field microscopy images as training data.

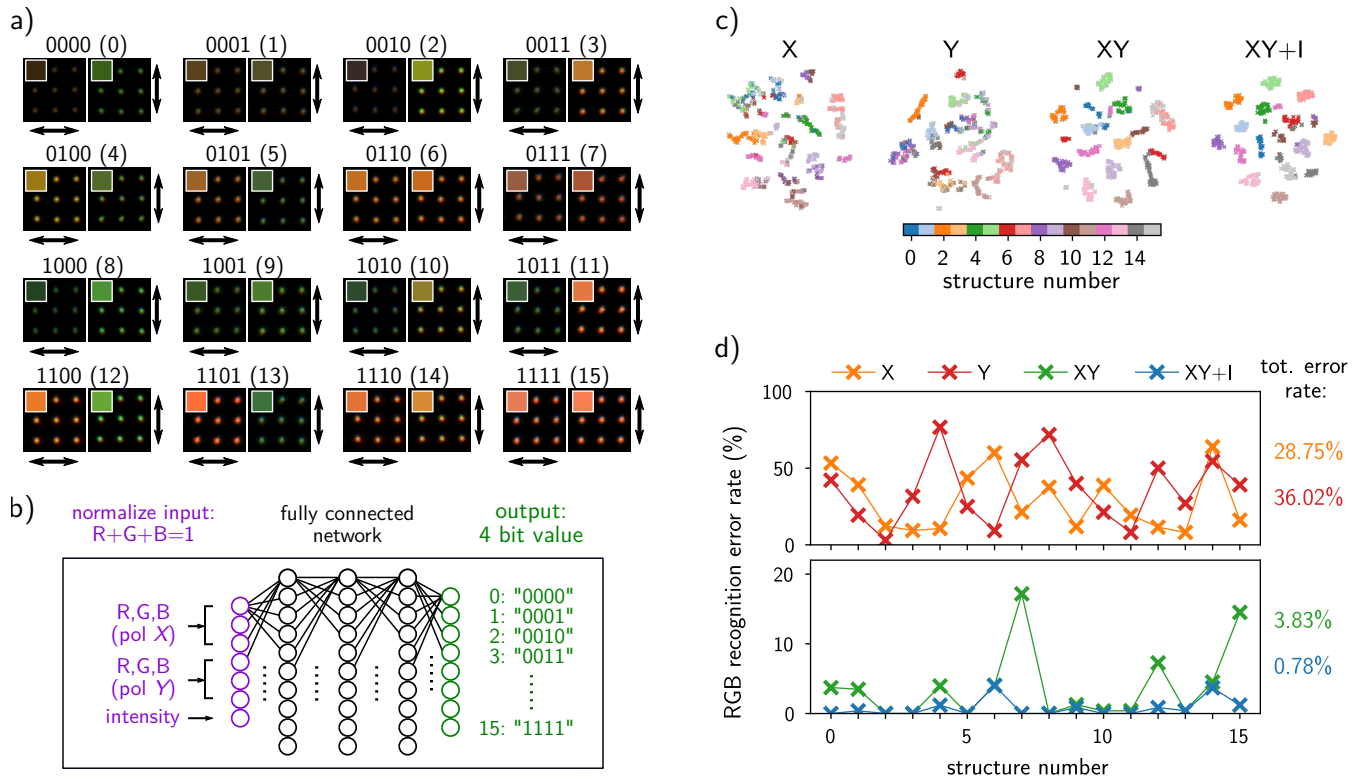


FIG. 4. **Neural-network based data read-out via the RGB color values.** (a) polarization filtered dark-field color images of representative 3×3 arrays of “4 bit” digit structures. Left: X -polarization, right: Y -polarization. The insets show the averaged RGB color of the 3×3 shown structures. (b) scheme of the fully connected artificial neural network used for the RGB classification task. (c) t-SNE³⁶ visualization of the different training sets. (d) information retrieval accuracy of the network, trained using data-sets consisting of only the X -filtered (orange), only the Y -filtered (red), $X+Y$ filtered (green) and XY filtered + the scattered intensities (blue).

1. Training data and network architecture

Figure 4a shows example DF images for each geometry and linear polarization. The subplots show arrays of 3×3 copies of the same 4-bit nanostructure, the average RGB color from the 9 structures in each plot is shown in a small square in the upper left corner of each plot. For the training dataset we use the average RGB values from the scattered light in the polarization filtered DF image, corresponding to one structure. We then normalize the RGB values to $R + G + B = 1$ and separately store the scattered intensity (hence the brightness). We create four training datasets: Three sets with only the normalized RGB information. One for X , one and for Y polarized data, as well as a third dataset combining both polarizations. The fourth set contains the XY spectra and additionally their brightness values (scattering intensity).

For the RGB datasets, we use an entirely fully connected network architecture, as depicted in Fig. 4b. Details on the technical implementation are given in the Methods section.

2. Results

The “t-SNE” plots and the read-out error rates for the test datasets are shown in figure 4c-d. The test data consists of polarization filtered RGB information for 4000 structures not seen during training. It seems that the X or Y polarized RGB values alone are not sufficient for an accurate identification of the structures. For those datasets the t-SNE distributions contain significant overlap of the different structure numbers and the average read-out error rates are unsatisfactorily high. The error rates of several individual binary numbers are even well above 50%.

However, using the datasets combining both polarizations, the situation drastically improves. The t-SNE plots (“ XY ” and “ $XY+I$ ”) now show a nice separation of the different binary numbers and the average error rate drops to 3.83% without the scattering intensity and can be reduced down to 0.78% when the brightness values are considered as well. In the latter case, the largest error rate is observed for the digits “0110” and “1110” (slightly below 4%, see blue lines in Fig. 4d), which scatter light in

a resembling orange tone, similar for both polarizations (see structures (6) and (14) in Fig.4a). The similarity can also be observed in the t-SNE plot “XY+I”, where some of the dark grey dots (structure “14”) are found very close to the saturated red points (structure “6”). By designing nanostructures with a more significant difference in the scattered colors (e.g. using modern inverse problem techniques^{16,37}), this limitation could be easily overcome and the error rate further decreased. In the [supporting informations](#), the activations of the neurons of the softmax output layer of the “RGB” network are shown for the whole validation sets of the “Y” and the “XY+I” cases.

The RGB color information technique is based on large-area microscopy images of the sample. Therefore it allows to simultaneously capture many thousands of structures within a single measurement, in other words it supports a massively parallel read-out of the information. Besides the dark-field illumination, the setup can in principle be fully implemented using cheap and mass-produced smart-phone components. Using specifically designed silicon bright-field color scatterers³⁸ for the information encoding, also the dark-field illumination could be replaced by a simple white light source, which renders the approach very attractive for mass-market perspectives.

III. TOWARDS HIGHER INFORMATION DENSITY

We demonstrated in the previous section that the knowledge of the full scattering spectrum of the “4 bit” nanostructures is not necessary to optically read-out the information. It is possible to retrieve the binary sequence simply via the RGB color of the scattered light. In consequence, with the more precise spectral read-out scheme, it should be possible to increase the information density of the individual nanostructures. To assess whether a larger amount of bits per structure can be accurately read by a deep neural network, we examine in the following the case of a “9 bit” nanostructure. The geometry is depicted in figure 5a. It consists of 3×3 silicon blocks of each $105 \text{ nm} \times 105 \text{ nm}$ width and length, leading to 512 possible structural arrangements. Two sides are surrounded by an L-shaped block of 45 nm width. The height of the structure is set to 90 nm, identical to the 4 bit nanostructures (see also figure 1a). We note that, unintentionally, increasing the size of the structures has a further, positive side-effect. In the 4 bit case, the red part of the spectra contains very little information (see figure 3b). Increasing the total size of the nanostructure moves the spectral features towards longer wavelengths and hence increases the information density in the red part of the spectra. This is advantageous for our aim to increase the information density to 9 bits per nanostructure.

1. Training data and network architecture

In order to perform a analysis of the read-out robustness at higher information densities, we study the 9 bit scenario on a synthetic dataset on which we can easily adjust the amount of noise in the spectra. We therefore numerically simulate the scattering spectra under X and Y polarized plane wave illumination for all 512 possible geometries using the Green Dyadic Method (GDM, see also Methods). We numerically add noise to the simulated spectra of each structure via a sequence of random modifications, as illustrated at the example of structure “001011010” (90) in figure 5b. First we add random noise (i), and apply a random positive offset (ii) as well as a scaling factor (iii). Then we multiply the spectra with a linear function of random slope (iv) and finally apply a wavelength-shift (v). In order to do so, in the first place we simulated the spectra on an extended wavelength range. Several of such modified spectra are shown in figure 5b(vi). The magnitude of the random variations can be adjusted to yield more or less strongly distorted results. Figure 5c shows several randomized spectra for noise magnitudes between 5% (i) and 25% (v). Our training set consists of 250 spectra per geometry and polarization, distorted using a noise magnitude of 10%. This leads to a total of $250 \cdot 2 \cdot 512 = 256000$ scattering spectra as training data.

We use the same 1D convolutional network architecture as in the “4 bit, spectral” case (see Methods).

2. Results

We test the trained network using separate datasets with 20 randomized X and Y spectra for each structure geometry, leading to a total of 10240 test structures. We generate test datasets with noise levels from 1% to 25%. The accuracy of the retrieval for these datasets is shown in figure 5d. The total average error rate is shown as a blue line, the error rate of the worst individual digit is shown in red. Because each digit is represented only by 20 different test-spectra, the minimum error in the “worst digit” plot is 5%, corresponding to one false assignment out of 20. The trained ANN retrieves the 10240 binary numbers without a single error until 9% of noise level, in which case the ANN incorrectly classifies two nanostructures in the test set (corresponding to an average error rate of 0.02%). Significant error rates start to occur only at noise levels around 15%. Some examples of false and correct classifications are given in the [supporting informations](#). The average error rate with 20% noise is still at a reasonable value of 4.16%. For the worst digit though, the error rate is as high as 35% in this case. An analysis of the error rate of the individual binary geometries at several noise levels is given in the [supporting informations](#). We note that the relatively high error rates on some specific digital numbers could be easily reduced by designing optically “more unique” nanostructures for the

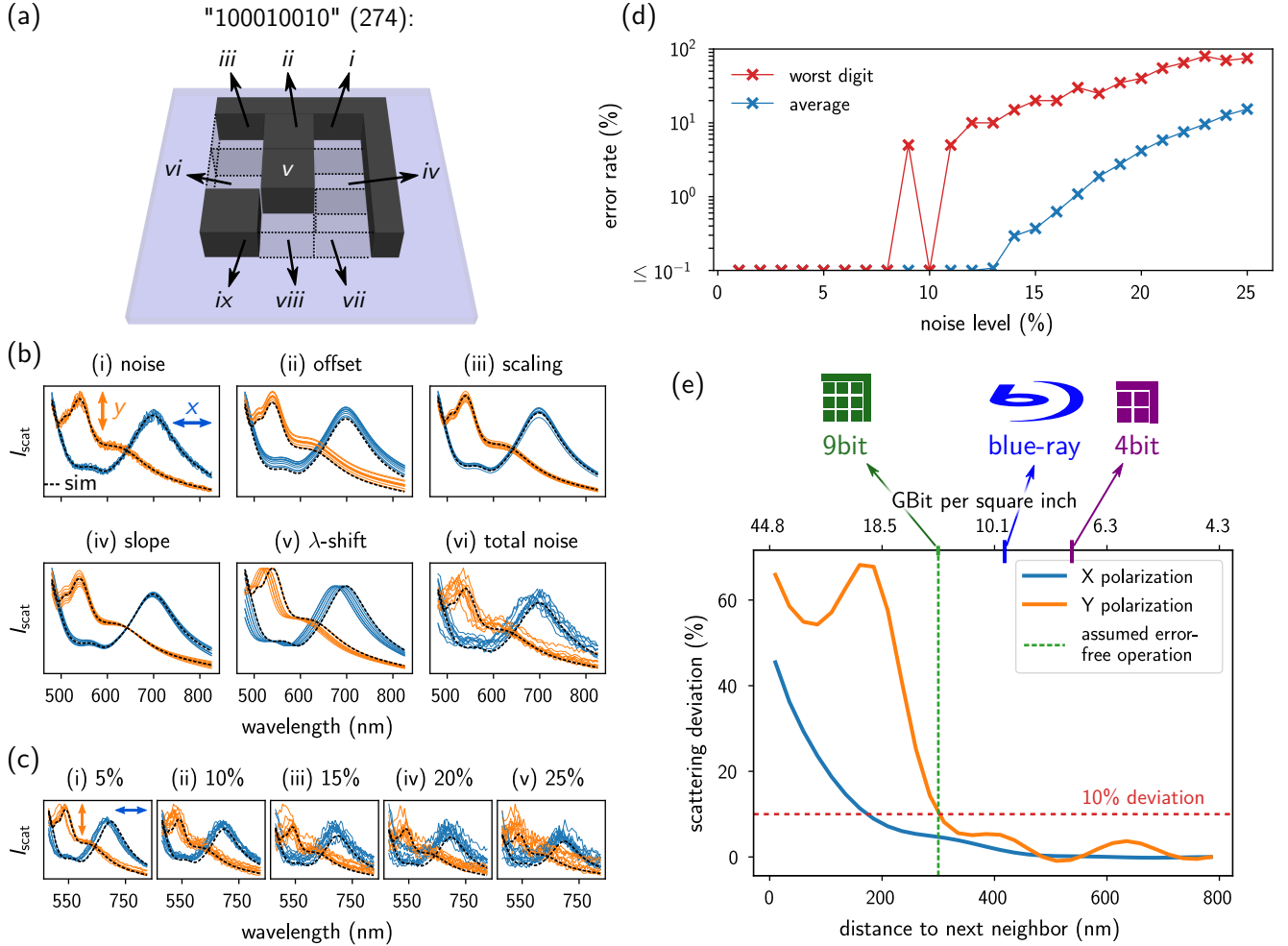


FIG. 5. **9 bit per nanostructure information encoding.** (a) geometry of the silicon nanostructure encoding $3 \times 3 = 9$ bits (512 possible combinations). The shown example represents the decimal number “274”. Each silicon block occupies an area of $105 \times 105 \text{ nm}^2$. The L-shaped sidewall is 45 nm wide. The height is 90 nm. (b) Training data generation from simulated spectra: add random (i) noise, (ii) a positive offset, (iii) a scaling factor, (iv) a slope and (v) a wavelength-shift. Several resulting spectra are shown in (vi) at the example of the spectra of digit “001011010” (decimal “90”). (c) several superposed example spectra for noise levels from (i) 5% to (v) 25%. (d) error rate as function of noise level. (e) scattering deviation relative to the isolated structure as function of the distance between two digit encoding structures for focused illumination. For the estimation of the feasible information density, 10% deviation from the unperturbed spectrum are assumed to be tolerable (red dashed horizontal line). This leads to an information density (green indicator) around 40% higher than the blue-ray disc (blue indicator). The 4 bit structures (purple indicator, see also experimental section) yield about 75% of the blue-ray density.

binary sequences with the high error rates.

Let’s finally compare the information density of the 9 bit nanostructures to the state-of-the art flat optical storage medium, the “blue-ray disc”. The blue-ray has a length and width per digit of 150 nm, respectively 130 nm, with 320 nm line spacing, leading to a required area $A_{1\text{bit}} = (320 + 130) \cdot 150 \text{ nm}^2 = 67500 \text{ nm}^2$ per bit. Our “9 bit” structures, require $(3 \cdot 105 + 45 + \text{spacing})^2 / 9 \text{ nm}^2$ per bit. In figure 5e we analyze the influence of a close neighbor on the scattering from a 9 bit nanostructure. Assuming a tolerable deviation of 10% compared to the isolated nanostructure’s spectrum,

a spacing of 300 nm would still allow an accurate read-out (see also [supporting informations](#)). This yields an around 40% higher information density compared to the blue-ray disc. With a 300 nm spacing, the 4 bit encoding nanostructures result in 75% of the blue-ray information density. Using properly designed sets of photonic nanostructures with highly distinguishable optical responses, the accuracy and robustness of the method can be straightforwardly further optimized. Also the area covered by each nanostructure could be decreased using a larger structure height than the above chosen 90 nm. Finally, the information per structure could possibly be

increased up to 11 or 12 bits (2048, respectively 4096 structure geometries), but larger binary sequences per structure seem difficult for an accurate read-out, due to the power-scaling by which the number of structure geometries increases ($2^{N_{\text{bit}}}$). Also multi-layer information storage could be possible in order to exploit – to a certain extent – all three spatial dimensions of a storage medium.^{22,23}

IV. CONCLUSIONS

In summary, we demonstrated on experimental data, that deep neural networks can be effectively trained for the optical retrieval of digital information, encoded in the geometry of photonic nanostructures. In the case of a binary sequence of 4 bits per nanostructure, the optical scattering spectra is more than sufficient for an accurate recovery of the encoded data. We showed that using simply the RGB color information, obtained from standard dark-field microscopy images, suffices to yield a precise read-out scheme. This approach allows a massively parallel retrieval of stored information on very simple and cheap equipment, potentially using smart-phone quality components. The read-out scheme could be even further simplified using specifically designed nanostructures for structural bright-field colors.³⁸ Also the information density can potentially be increased by employing nanostructure geometries with tailored, high color-contrast.³⁹

Using the full scattering spectrum, we demonstrated that the information density can be significantly further increased. We trained an artificial neural network on a numerical dataset of nanostructures encoding 9 bits of binary information each. Even for fairly large amounts of noise in the scattering spectra, almost error-free retrieval of the binary data is possible at information densities outperforming the blue-ray disc, which to date offers the highest commercially available density. Practical read-out schemes in the high-information density case could be realized using compressed, hence spectrally broad, femtosecond laser pulses¹⁷ or supercontinuum lasers.

Our work paves the way towards accurate and massively parallel read-out of high density planar optical information storage using simple far-field characterization techniques and concepts of modern machine learning. Re-writeable storage media might be created around the recently developed technology on catalytic magnesium metasurfaces for the dynamic adaptation of structural color.⁴⁰ Our approach can be easily generalized to other classification tasks in nano-optics, including applications in plasmonics or in the identification of biological specimen.

ACKNOWLEDGMENTS

We gratefully thank Arnaud Arbouet and Christian Girard for their inspiring advise, their valuable help and

for proof-reading the manuscript. We also thank Vincent Paillard and Aurélien Cuche for fruitful discussions and for proof-reading the manuscript. This work was supported by Programme Investissements d’Avenir under the program ANR-11-IDEX-0002-02, reference ANR-10-LABX-0037-NEXT, by the LAAS-CNRS micro and nanotechnologies platform, a member of the French RENATECH network and by the computing facility center CALMIP of the University of Toulouse under grant P12167.

AUTHOR CONTRIBUTIONS

P.R.W. conceived the idea and designed the research together with G.L. G.L. and A.L. developed the fabrication techniques. A.L. and N.M. fabricated the nanostructures and performed the electron microscopy. P.R.W. carried out the optical experiments, did the simulations, the data analysis and implemented the machine learning part. P.R.W. wrote the manuscript with contributions from G.L. All authors discussed the results and commented on the manuscript at every stage.

ADDITIONAL INFORMATION

Supplementary information is available in the online version of the paper. Reprints and permission information is available online at www.nature.com/reprints. Correspondence and requests for materials should be addressed to P.R.W.

COMPETING FINANCIAL INTERESTS

The authors declare no competing financial interests.

V. METHODS

A. Nanofabrication of planar Si structures

The silicon nanostructures were patterned on silicon on insulator (SOI) substrate (90 nm active Si layer on 30 nm buried oxide) following a large scale top-down approach. Electron beam lithography was used to pattern 80 nm thick layer of an inorganic negative-tone resist, namely hydrogen silsesquioxane (HSQ). After exposure, HSQ was developed by immersion in 25% tetramethylammonium hydroxide (TMAH) for one minute.⁴¹ HSQ patterns were subsequently transferred to the silicon substrate down to the buried oxide by anisotropic reactive ion etching (RIE). Then, the structures were embedded in a 200 nm thick HSQ layer, deposited by spin coating in order to perfectly planarize the sample in a nanometrical range.⁴² Finally, the HSQ layer (SiO_xH_y) was converted into a SiO_x layer by rapid thermal annealing at 600°C /

2 min under nitrogen ambiance, leading to a final SiO_x thickness layer of 190 nm.

B. Confocal dark-field microscopy

The scattering spectra were acquired out on a confocal dark-field microscope (Horiba XploRA). A white lamp was focused on the sample by a $\times 50$ dark-field objective (NA 0.5, condenser: NA 0.8 – 0.95). The backscattered light was filtered by a confocal hole (diameter of 100 μm) and a polarization filter and dispersed by a grating (300 grooves mm^{-1}) on a Peltier-cooled CCD. The acquisition time was 0.5s. All spectra were normalized by the spectrum of the lamp.

The polarization filtered dark-field images were taken using the same $\times 50$ DF microscope objective, with a color CCD camera at a resolution of 1392×1040 and an exposure time of 0.05s. Each structure is perceived as a colored dot on the microscopy image, covering $\approx 20 - 50$ pixels, from which we take the average RGB value.

C. Electrodynamical simulations

The numerical simulations for the 9-bit structures are performed using the Green Dyadic Method (GDM), a frequency-domain approach based on the concept of a generalized propagator.⁴³ In particular, we use an own implementation in python, “pyGDM”.⁴⁴

In the GDM the volume of a nanostructure is discretized with N cubic meshpoints of edge length d . To each of these mesh-points, a dipolar response is attributed. As detailed e.g. in reference⁴⁵, this leads to a system of $3N$ coupled equations

$$\mathbf{E}_0 = \mathbf{M} \cdot \mathbf{E}, \quad (1)$$

which, by inversion of \mathbf{M} , allows to relate any incident electric field \mathbf{E}_0 to the induced field \mathbf{E} inside the particle. \mathbf{M} is composed of 3×3 sub-matrices

$$\mathbf{M}_{ij} = \mathbf{I} \delta_{ij} - \alpha_i(\omega) \mathbf{G}(\mathbf{r}_i, \mathbf{r}_j, \omega). \quad (2)$$

\mathbf{I} is the Cartesian unitary tensor, δ_{ij} the Kronecker delta function and, in cgs units,

$$\alpha_i(\omega) = \frac{\epsilon_i(\omega) - \epsilon_{\text{env}}(\omega)}{4\pi} v_i. \quad (3)$$

In the latter equation, v_i is the volume of the cubic discretization cells hence $v_i = d^3$. We use the dispersion of silicon from Palik⁴⁶ for ϵ_i . The structures are placed in a homogeneous environment ($\epsilon_{\text{env}} = 1.45$ for SiO_2) at 30 nm above a silicon substrate.

\mathbf{G} in Eq. (2) is the Green’s Dyad, coupling the cubic meshpoints i and j . It is composed of a vacuum term (accounting for the homogeneous environment) and a surface term (accounting for the substrate):

$$\mathbf{G}(\mathbf{r}_i, \mathbf{r}_j, \omega) = \mathbf{G}_0(\mathbf{r}_i, \mathbf{r}_j, \omega) + \mathbf{G}_{\text{surf}}(\mathbf{r}_i, \mathbf{r}_j, \omega) \quad (4)$$

which can be found in literature.⁴⁵ At $\mathbf{r}_i = \mathbf{r}_j$ the Green’s Dyad \mathbf{G}_0 diverges, hence a normalization scheme is applied:

$$\mathbf{G}_0(\mathbf{r}_i, \mathbf{r}_i, \omega) = \mathbf{I} C(\omega). \quad (5)$$

For a cubic mesh we use⁴⁵

$$C(\omega) = -\frac{4\pi}{3} \frac{1}{\epsilon_{\text{env}}(\omega) v_i}. \quad (6)$$

We invert equation (1) using LU-decomposition, the scattering cross-sections can be calculated from the near-field \mathbf{E} inside the particle.⁴⁷ We note that the GDM allows also to consider periodic structures⁴⁸ which is in particular interesting for metasurface simulations.⁴⁹

D. Training artificial neural networks for spectrum-based classification

The artificial neural networks are implemented in python using the tensorflow package.⁵⁰

Digit retrieval using scattering spectra – 1D ConvNet

Preprocessing of scattering spectra Prior to the training of the ANN, we pre-process the acquired scattering spectra. After background subtraction and normalization to the spectrum of the white lamp, we apply the following, further processing steps on our data. We first apply a median filter with 6 nm kernel size to eliminate spikes from the spectra. Subsequently we apply a smoothing filter based on moving averages with a 15 nm kernel to reduce the noise. We finally apply a down-sampling procedure using an order 8 Chebyshev type I filter by which we reduce the number of wavelengths to 99 per spectrum.

Network architecture The scattering spectra based network for information retrieval is a one-dimensional convolutional network followed by a fully connected part. The ConvNet consists of three layers using the “leaky ReLU” activation function. The first layer with 64 filters per channel uses a kernel of size 7. The second and third layers both have 32 filters with kernels of size 5 and 3, respectively. Each 1D convolutional layer is followed by a max pooling layer with kernel size 2 as well as by a batch normalization.⁵¹ The fully connected network consists of two layers with 64 and 32 neurons, employing a “tanh” activation. For the ConvNet part, we apply an “L2” regularization, for the fully connected part a dropout regularization scheme with 80% keep probability. We train the network as depicted in Fig. 1d using a variant of the stochastic gradient descent (SGD) algorithm (“Adam”, for details see Ref. 52) with a batch size of 64. We use the categorical cross-entropy loss, a learning rate of 0.0001 and train the network for 200 epochs. In the case of the 9 bit structures we train the network for 2000 epochs.

Preprocessing of scattering spectra We automatically process the polarization filtered darkfield microscopy images by considering all pixels with a brightness of at least $3\times$ the background level. Using this procedure, each structure results in a dot of 30-50 pixels in the DF images. Our dataset is composed of the average RGB values of the ensemble of pixels corresponding to each nanostructure. We normalize the RGB values to $R + G + B = 1$ and separately store the scattered intensity (hence the brightness).

Network architecture We use a fully connected network for the RGB datasets. The R, G, B (and possibly intensity) values are the input to the network, which itself consist of three layers with “tanh” activation in the following order: 128, 256 and 64 artificial neurons. We use L2 regularization and dropout with 80% keep probability on the entire ANN. The 16 neurons in the “softmax” output layer represent the binary numbers encoded in the nanostructures. We train the network on RGB data from 4800 nanostructures, using the original SDG algorithm and the categorical cross-entropy loss function. The batch size is 64. The learning rate is 1.0 with a $\times 0.96$ decay each 1000 steps (\approx each 13 epochs).

-
- ¹ J. Zhang, M. Gecevičius, M. Beresna, and P. G. Kazansky, *Physical Review Letters* **112**, 033901 (2014).
 - ² M. Gu, X. Li, and Y. Cao, *Light: Science & Applications* **3**, e177 (2014).
 - ³ I. Satoh, S. Ohara, N. Akahira, and M. Takenaga, *IEEE Transactions on Magnetics* **34**, 337 (1998).
 - ⁴ H. J. Borg, M. van Schijndel, J. C. N. Rijpers, M. H. R. Lankhorst, G. Zhou, M. J. Dekker, I. P. D. Ubbens, and M. Kuijper, *Japanese Journal of Applied Physics* **40**, 1592 (2001).
 - ⁵ B. J. Zeng, R. W. Ni, J. Z. Huang, Z. Li, and X. S. Miao, *Journal of Optics* **16**, 125402 (2014).
 - ⁶ J. Tominaga, T. Nakano, and N. Atoda, *Applied Physics Letters* **73**, 2078 (1998).
 - ⁷ M. D. Mottaghi and C. Dwyer, *Advanced Materials* **25**, 3593 (2013).
 - ⁸ J. H. Strickler and W. W. Webb, *Optics Letters* **16**, 1780 (1991).
 - ⁹ P. J. van Heerden, *Applied Optics* **2**, 393 (1963).
 - ¹⁰ D. Psaltis and G. W. Burr, *Computer* **31**, 52 (1998).
 - ¹¹ C. Girard, *Reports on Progress in Physics* **68**, 1883 (2005).
 - ¹² L. Novotny and B. Hecht, *Principles of Nano-Optics* (Cambridge University Press, Cambridge ; New York, 2006).
 - ¹³ S. Maier, *Plasmonics: Fundamentals and Applications* (Springer US, 2010).
 - ¹⁴ A. I. Kuznetsov, A. E. Miroschnichenko, M. L. Brongersma, Y. S. Kivshar, and B. Luk'yanchuk, *Science* **354** (2016), 10.1126/science.aag2472.
 - ¹⁵ L. Cao, P. Fan, E. S. Barnard, A. M. Brown, and M. L. Brongersma, *Nano Letters* **10**, 2649 (2010).
 - ¹⁶ P. R. Wiecha, A. Arbouet, C. Girard, A. Lecestre, G. Larrieu, and V. Paillard, *Nature Nanotechnology* **12**, 163 (2017).
 - ¹⁷ M. Mansuripur, A. R. Zakharian, A. Lesuffleur, S.-H. Oh, R. J. Jones, N. C. Lindquist, H. Im, A. Kobayakov, and J. V. Moloney, *Optics Express* **17**, 14001 (2009).
 - ¹⁸ W. T. Chen, P. C. Wu, C. J. Chen, C.-J. Weng, H.-C. Lee, T.-J. Yen, C.-H. Kuan, M. Mansuripur, and D. P. Tsai, *Applied Physics Letters* **98**, 171106 (2011).
 - ¹⁹ Y. Cui, I. Y. Phang, R. S. Hegde, Y. H. Lee, and X. Y. Ling, *ACS Photonics* **1**, 631 (2014).
 - ²⁰ M. A. El-Rabiaey, N. F. F. Areed, and S. S. A. Obayya, *Journal of Lightwave Technology* **34**, 3726 (2016).
 - ²¹ P. Zijlstra, J. W. M. Chon, and M. Gu, *Nature* **459**, 410 (2009).
 - ²² A. B. Taylor, J. Kim, and J. W. M. Chon, *Optics Express* **20**, 5069 (2012).
 - ²³ A. B. Taylor, P. Michaux, A. S. M. Mohsin, and J. W. M. Chon, *Optics Express* **22**, 13234 (2014).
 - ²⁴ X. Li, Y. Cao, N. Tian, L. Fu, and M. Gu, *Optica* **2**, 567 (2015).
 - ²⁵ D. Liu, Y. Tan, E. Khoram, and Z. Yu, *ACS Photonics* (2018), 10.1021/acsp Photonics.7b01377.
 - ²⁶ P. Albella, M. A. Poyli, M. K. Schmidt, S. A. Maier, F. Moreno, J. J. Sáenz, and J. Aizpurua, *The Journal of Physical Chemistry C* **117**, 13573 (2013).
 - ²⁷ M. A. Nielsen, *Neural Networks and Deep Learning* (Determination Press, 2015).
 - ²⁸ I. Goodfellow, Y. Bengio, and A. Courville, *Deep Learning* (MIT Press, 2016).
 - ²⁹ C. Szegedy, S. Ioffe, V. Vanhoucke, and A. Alemi, arXiv:1602.07261 [cs] (2016), arXiv:1602.07261 [cs].
 - ³⁰ P. Mamoshina, A. Vieira, E. Putin, and A. Zhavoronkov, *Molecular Pharmaceutics* **13**, 1445 (2016).
 - ³¹ T. Shimobaba, N. Kuwata, M. Homma, T. Takahashi, Y. Nagahama, M. Sano, S. Hasegawa, R. Hirayama, T. Kakue, A. Shiraki, N. Takada, and T. Ito, *Applied Optics* **56**, 7327 (2017).
 - ³² Y. Jo, S. Park, J. Jung, J. Yoon, H. Joo, M.-h. Kim, S.-J. Kang, M. C. Choi, S. Y. Lee, and Y. Park, *Science Advances* **3**, e1700606 (2017).
 - ³³ I. Malkiel, A. Nagler, M. Mrejen, U. Arieli, L. Wolf, and H. Suchowski, arXiv:1702.07949 [physics] (2017), arXiv:1702.07949 [physics].
 - ³⁴ J. Peurifoy, Y. Shen, L. Jing, Y. Yang, F. Cano-Renteria, B. Delacy, M. Tegmark, J. D. Joannopoulos, and M. Soljacic, arXiv:1712.03222 [physics] (2017), arXiv:1712.03222 [physics].
 - ³⁵ An “epoch” is a ML term, signifying one full training iteration. In each epoch, the full training dataset is randomly shuffled and used in its totality to optimize the network parameters.
 - ³⁶ L. van der Maaten and G. Hinton, *Journal of Machine Learning Research* **9**, 2579 (2008).
 - ³⁷ T. Feichtner, O. Selig, M. Kiumke, and B. Hecht, *Physical Review Letters* **109**, 127701 (2012).
 - ³⁸ V. Flauraud, M. Reyes, R. Paniagua-Domínguez, A. I. Kuznetsov, and J. Brugger, *ACS Photonics* (2017), 10.1021/acsp Photonics.6b01021.

- ³⁹ A. K. González-Alcalde, R. Salas-Montiel, H. Mohamad, A. Morand, S. Blaize, and D. Macías, *Applied Optics* **57**, 3959 (2018).
- ⁴⁰ X. Duan, S. Kamin, and N. Liu, *Nature Communications* **8**, 14606 (2017).
- ⁴¹ Y. Guerfi, F. Carcenac, and G. Larrieu, *Microelectronic Engineering* **110**, 173 (2013).
- ⁴² Y. Guerfi, J. B. Doucet, and G. Larrieu, *Nanotechnology* **26**, 425302 (2015).
- ⁴³ O. J. F. Martin, C. Girard, and A. Dereux, *Physical Review Letters* **74**, 526 (1995).
- ⁴⁴ P. R. Wiecha, arXiv:1802.04071 (2018), [arXiv:1802.04071](https://arxiv.org/abs/1802.04071).
- ⁴⁵ C. Girard, E. Dujardin, G. Baffou, and R. Quidant, *New Journal of Physics* **10**, 105016 (2008).
- ⁴⁶ D. F. Edwards, in *Handbook of Optical Constants of Solids*, edited by E. D. Palik (Academic Press, Burlington, 1997) pp. 547 – 569.
- ⁴⁷ B. T. Draine, *Astrophysical Journal* **333**, 848 (1988).
- ⁴⁸ B. Gallinet and O. J. F. Martin, *Theoretical And Computational Nanophotonics (Tacona-Photonics 2009)* **1176**, 63 (2009).
- ⁴⁹ C. Yan, K.-Y. Yang, and O. J. F. Martin, *Light: Science & Applications* **6**, e17017 (2017).
- ⁵⁰ M. Abadi, A. Agarwal, P. Barham, E. Brevdo, Z. Chen, C. Citro, G. S. Corrado, A. Davis, J. Dean, M. Devin, S. Ghemawat, I. Goodfellow, A. Harp, G. Irving, M. Isard, Y. Jia, R. Jozefowicz, L. Kaiser, M. Kudlur, J. Levenberg, D. Mané, R. Monga, S. Moore, D. Murray, C. Olah, M. Schuster, J. Shlens, B. Steiner, I. Sutskever, K. Talwar, P. Tucker, V. Vanhoucke, V. Vasudevan, F. Viégas, O. Vinyals, P. Warden, M. Wattenberg, M. Wicke, Y. Yu, and X. Zheng, <https://www.tensorflow.org/> (2015).
- ⁵¹ S. Ioffe and C. Szegedy, arXiv:1502.03167 [cs] (2015), [arXiv:1502.03167 \[cs\]](https://arxiv.org/abs/1502.03167).
- ⁵² D. P. Kingma and J. Ba, arXiv:1412.6980 [cs] (2014), [arXiv:1412.6980 \[cs\]](https://arxiv.org/abs/1412.6980).